

ALMA chemical survey of disk-outflow sources in Taurus (ALMA-DOT). IV. Thioformaldehyde (H2CS) in protoplanetary discs: spatial distributions and binding energies

C. Codella, L. Podio, A. Garufi, J. Perrero, P. Ugliengo, D. Fedele, C. Favre, E. Bianchi, C. Ceccarelli, S. Mercimek, et al.

▶ **To cite this version:**

C. Codella, L. Podio, A. Garufi, J. Perrero, P. Ugliengo, et al.. ALMA chemical survey of disk-outflow sources in Taurus (ALMA-DOT). IV. Thioformaldehyde (H2CS) in protoplanetary discs: spatial distributions and binding energies. Astronomy and Astrophysics - A&A, 2020, 644, 10.1051/0004-6361/202039309 . insu-03705166

HAL Id: insu-03705166
https://insu.hal.science/insu-03705166

Submitted on 27 Jun 2022

HAL is a multi-disciplinary open access archive for the deposit and dissemination of scientific research documents, whether they are published or not. The documents may come from teaching and research institutions in France or abroad, or from public or private research centers.

L'archive ouverte pluridisciplinaire **HAL**, est destinée au dépôt et à la diffusion de documents scientifiques de niveau recherche, publiés ou non, émanant des établissements d'enseignement et de recherche français ou étrangers, des laboratoires publics ou privés.

A&A 644, A120 (2020)
https://doi.org/10.1051/0004-6361/202039309
© ESO 2020

Astronomy & Astrophysics

ALMA chemical survey of disk-outflow sources in Taurus (ALMA-DOT)

IV. Thioformaldehyde (H_2CS) in protoplanetary discs: spatial distributions and binding energies*

C. Codella[1,2], L. Podio[1], A. Garufi[1], J. Perrero[3], P. Ugliengo[3], D. Fedele[1,4], C. Favre[2], E. Bianchi[2], C. Ceccarelli[2], S. Mercimek[1,5], F. Bacciotti[1], K. L. J. Rygl[6], and L. Testi[7,8,1]

[1] INAF, Osservatorio Astrofisico di Arcetri, Largo E. Fermi 5, 50125 Firenze, Italy
e-mail: codella@arcetri.astro.it
[2] Univ. Grenoble Alpes, CNRS, Institut de Planétologie et d'Astrophysique de Grenoble (IPAG), 38000 Grenoble, France
[3] Dipartimento di Chimica and Nanostructured Interfaces and Surfaces (NIS) Centre, Università degli Studi di Torino, Via P. Giuria 7, 10125 Torino, Italy
[4] INAF, Osservatorio Astrofisico di Torino, Via Osservatorio 20, 10025 Pino Torinese, Italy
[5] Università degli Studi di Firenze, Dipartimento di Fisica e Astronomia, Via G. Sansone 1, 50019 Sesto Fiorentino, Italy
[6] INAF, Istituto di Radioastronomia & Italian ALMA Regional Centre, Via P. Gobetti 101, 40129 Bologna, Italy
[7] European Southern Observatory, Karl-Schwarzschild-Strasse 2, 85748 Garching bei München, Germany
[8] Excellence Cluster Origins, Boltzmannstrasse 2, 85748 Garching bei München, Germany

Received 1 September 2020 / Accepted 2 November 2020

ABSTRACT

Context. Planet formation starts around Sun-like protostars with ages ≤1 Myr, but the chemical compositions of the surrounding discs remains unknown.
Aims. We aim to trace the radial and vertical spatial distribution of a key species of S-bearing chemistry, namely H_2CS, in protoplanetary discs. We also aim to analyse the observed distributions in light of the H_2CS binding energy in order to discuss the role of thermal desorption in enriching the gas disc component.
Methods. In the context of the ALMA chemical survey of disk-outflow sources in the Taurus star forming region (ALMA-DOT), we observed five Class I or early Class II sources with the o-$H_2CS(7_{1,6}-6_{1,5})$ line. ALMA-Band 6 was used, reaching spatial resolutions ≃40 au, that is, Solar System spatial scales. We also estimated the binding energy of H_2CS using quantum mechanical calculations, for the first time, for an extended, periodic, crystalline ice.
Results. We imaged H_2CS emission in two rotating molecular rings in the HL Tau and IRAS 04302+2247 discs, the outer radii of which are ∼140 au (HL Tau) and 115 au (IRAS 04302+2247). The edge-on geometry of IRAS 04302+2247 allows us to reveal that H_2CS emission peaks at radii of 60–115 au, at $z = \pm 50$ au from the equatorial plane. Assuming LTE conditions, the column densities are $\sim 10^{14}$ cm^{-2}. We estimate upper limits of a few 10^{13} cm^{-2} for the H_2CS column densities in DG Tau, DG Tau B, and Haro 6–13 discs. For HL Tau, we derive, for the first time, the [H_2CS]/[H] abundance in a protoplanetary disc ($\simeq 10^{-14}$). The binding energy of H_2CS computed for extended crystalline ice and amorphous ices is 4258 and 3000–4600 K, respectively, implying thermal evaporation where dust temperatures are ≥50–80 K.
Conclusions. H_2CS traces the so-called warm molecular layer, a region previously sampled using CS and H_2CO. Thioformaldehyde peaks closer to the protostar than H_2CO and CS, plausibly because of the relatively high excitation level of the observed $7_{1,6}-6_{1,5}$ line (60 K). The H_2CS binding energy implies that thermal desorption dominates in thin, au-sized, inner and/or upper disc layers, indicating that the observed H_2CS emitting up to radii larger than 100 au is likely injected in the gas phase due to non-thermal processes.

Key words. astrochemistry – protoplanetary disks – methods: numerical – ISM: individual objects: HL Tau – ISM: individual objects: IRAS 04302+2247

1. Introduction

Low-mass star formation is the process starting from a molecular cloud and ending with a Sun-like star with its own planetary system. According to the classical scenario (e.g. Andre et al. 2000; Caselli & Ceccarelli 2012, and references therein), the central object increases its mass through an accretion disc, while a fast jet contributes in removing the angular momentum excess. While the star accretes its mass, part of the material in the disc is incorporated to form planets. As the physical process proceeds, the chemistry evolves towards a complex gas composition (see Ceccarelli et al. 2007; Herbst & van Dishoeck 2009). Several observational programs have been dedicated to the chemical content of protostellar envelopes/discs using both single-dish radiotelescopes and interferometers at millimetre(mm) wavelenghts (IRAM 30-m ASAI, Lefloch et al. 2018; ALMA PILS, Jørgensen et al. 2016; IRAM PdBI CALYPSO,

* Reduced datacubes are only available at the CDS via anonymous ftp to cdsarc.u-strasbg.fr (130.79.128.5) or via http://cdsarc.u-strasbg.fr/viz-bin/cat/J/A+A/644/A120

Belloche et al. 2020; IRAM NOEMA SOLIS, Ceccarelli et al. 2017; ALMA FAUST[1], Bianchi et al. 2020); the recent IRAM 30-m survey by Le Gal et al. (2020). Nevertheless, relatively little is known about the chemical content of the protoplanetary discs. Tiny outer molecular layers (and therefore small column densities) are formed due to thermal or UV-photodesorption and/or CR-induced desorption (e.g., Semenov & Wiebe 2011; Walsh et al. 2014, 2016; Loomis et al. 2015; Le Gal et al. 2019). More precisely, the disc portions where thermal desorption is expected to rule are in turn determined by the binding energies (BEs) of the species to grains. Different BEs imply different temperatures of the dust which can inject frozen molecules into the gas phase (e.g. Penteado et al. 2017).

Several projects focusing on protoplanetary discs, mainly with ALMA[2], have recently come to fruition, leading to the detection of several molecules from CO isotopologues to complex species such as t-HCOOH, CH_3OH, and CH_3CN (see Öberg et al. 2013, 2015a,b; Öberg & Bergin 2016; Guilloteau et al. 2016; Favre et al. 2015, 2018, 2019; Fedele et al. 2017; Semenov et al. 2018; Podio et al. 2019, 2020a,b; Garufi et al. 2020). The ALMA images allowed these latter authors to compare the gas and dust distribution, making the first steps in physical–chemical modelling. A breakthrough result provided by ALMA, through (sub)mm array observations of young stellar objects, suggests that planets already start to form during the protostellar phases, that is, before the classical protoplanetary stage at an age of at least 1 Myr. This is indirectely indicated by the presence of rings, gaps, and spirals in discs with ages of less than 1 Myr (see e.g., Sheehan & Eisner 2017; Fedele et al. 2018; Andrews et al. 2018). These substructures have also been observed using molecules, driving studies to sample the molecular components of discs. This is the goal of the ALMA-DOT project (ALMA chemical survey of Disk-Outflow sources in Taurus), which targets Class I or early Class II discs to obtain their chemical characterisation.

The chemistry of S-bearing species is not well understood. In dense gas, which is involved in the star forming process, sulphur is severely depleted (e.g. Wakelam et al. 2004; Phuong et al. 2018; Tieftrunk et al. 1994; Laas & Caselli 2019; van 't Hoff et al. 2020), that is, by at least two orders of magnitude with respect to the Solar System value $[S]/[H] = 1.8 \times 10^{-5}$ (Anders & Grevesse 1989). However, the main S-carrier species on dust grains are still unknown. For years, H_2S has been postulated to be the solution, but so far it has not been directly detected on interstellar ices (Boogert et al. 2015). Alternative solutions have been proposed in light of studies focused on protostellar shocks, where dust is sputtered: S, OCS, and H_2CS (e.g. Wakelam et al. 2004; Codella et al. 2005; Podio et al. 2014; Holdship et al. 2016) have been investigated, but again no detection on ices has been reported (Boogert et al. 2015). Regarding the inventory of S-molecules in protoplanetary discs, only four species have been detected, often using single-dish radiotelescopes: CS, SO, H_2S, and H_2CS. More specifically, multiline CS emission has been observed towards approximately ten discs (e.g. Dutrey et al. 1997, 2017; Fuente et al. 2010; Guilloteau et al. 2013, 2016; Teague et al. 2018; Phuong et al. 2018; Semenov et al. 2018; Le Gal et al. 2019; Garufi et al. 2020; Podio et al. 2020a). SO emission has been detected in fewer discs, some of them still associated with accretion, such as for example TMC-1A (e.g. Fuente et al. 2010; Guilloteau et al. 2013, 2016; Sakai et al. 2016; Pacheco-Vázquez et al. 2016; Teague et al. 2018; Booth et al. 2018). On the other hand, only very recently, H_2S and H_2CS were detected and imaged towards multiple discs. Namely, H_2S was imaged towards GG Tau A (Phuong et al. 2018), while H_2CS was observed with ALMA towards MWC480, and, tentatively, LkCa 15 (Le Gal et al. 2019; Loomis et al. 2020). Further observations of the most likely dust-grain S-carriers are required in the interest of a definitive conclusion.

In this context, the goal of the present project is twofold: (1) to map the H_2CS (thioformaldehyde) spatial distribution in protoplanetary discs in an intermediate phase between Class I and Class II, and (2) to derive the binding energies of H_2CS using quantum mechanical calculations for an extended crystalline ice. We focus on H_2CS in an effort to identify S-bearing species able to trace protoplanetary discs. The present article is organised as follows. We first present our observations and data reduction process (Sect. 2), followed by our observational results (Sect. 3) and the methods and assumptions we used to derive BEs (Sect. 4). In Sect. 5, we discuss our results by comparing the H_2CS maps with (i) those of other molecular species and with (ii) the spatial distributions expected when assuming the thermal desorption process (driven by the BE values) to be the main mechanism leading to H_2CS in the gas phase. Finally, Sect. 6 summarises our work.

2. Observations: sample and data reduction

The sample consists of four well-known Class I and one early Class II (e.g. Andre et al. 2000) sources (Guilloteau et al. 2013, 2014): DG Tau, DG Tau B, HL Tau, IRAS 04302+2247, and Haro 6–13 (also known as V 806 Tau). The sources are observed in the context of the ALMA-DOT project, which targets sources: (i) still embedded in a dense envelope and (ii) driving an atomic jet and a molecular outflow. The sources are chemically rich as revealed by IRAM-30m observations detecting CO isotopologues, H_2CO, and CN – plus SO for all but Haro 6–13 – (Guilloteau et al. 2013).

This work is based on ALMA Cycle 4 observations of DG Tau and DG Tau B and Cycle 6 observations of HL Tau, IRAS 04302+2247, and Haro 6-13 (projects 2016.1.00846.S and 2018.1.01037.S, PI: L. Podio). The DG Tau and DG Tau B observations were described by Podio et al. (2019), and Garufi et al. (2020), respectively. All Band 6 observations were taken in an extended array configuration with baselines ranging from 15 m to 1.4 km or from 17 m to 3.7 km. The frequency interval covered by the continuum spectral window included the o–$H_2CS(7_{1,6}-6_{1,5})$ line emitting at 244 048.5 MHz, characterised[3] by $E_{up} = 60$ K, and $S\mu^2 = 56$ D^2. A standard data reduction was performed with CASA pipeline version 4.7.2. Self-calibration was performed on the continuum emission and then applied to the continuum-subtracted line datacube. The rms for continuum images are about 68 μJy (HL Tau) and 40 μJy (IRAS 04302+2247). The line spectral cube was produced through TCLEAN. We used robust weighting in order to maximise the spatial resolution, and set a channel width of 1.2 km s^{-1}. The r.m.s. per each channel is about 0.8 mJy beam^{-1}. The synthesised beam (HPBW) is $\sim 0\farcs3 \times 0\farcs3$.

3. Observational results

3.1. Continuum and H_2CS spatial distributions

Out of the five observed targets, we detected o-$H_2CS(7_{1,6}-6_{1,5})$ emission towards two discs, namely HL Tau and

[1] http://faust-alma.riken.jp

[2] Atacama Large Millimeter Array: https://www.almaobservatory.org

[3] The spectral parameters (Maeda et al. 2008) are taken from the Cologne Database for Molecular Spectroscopy (Müller et al. 2005).

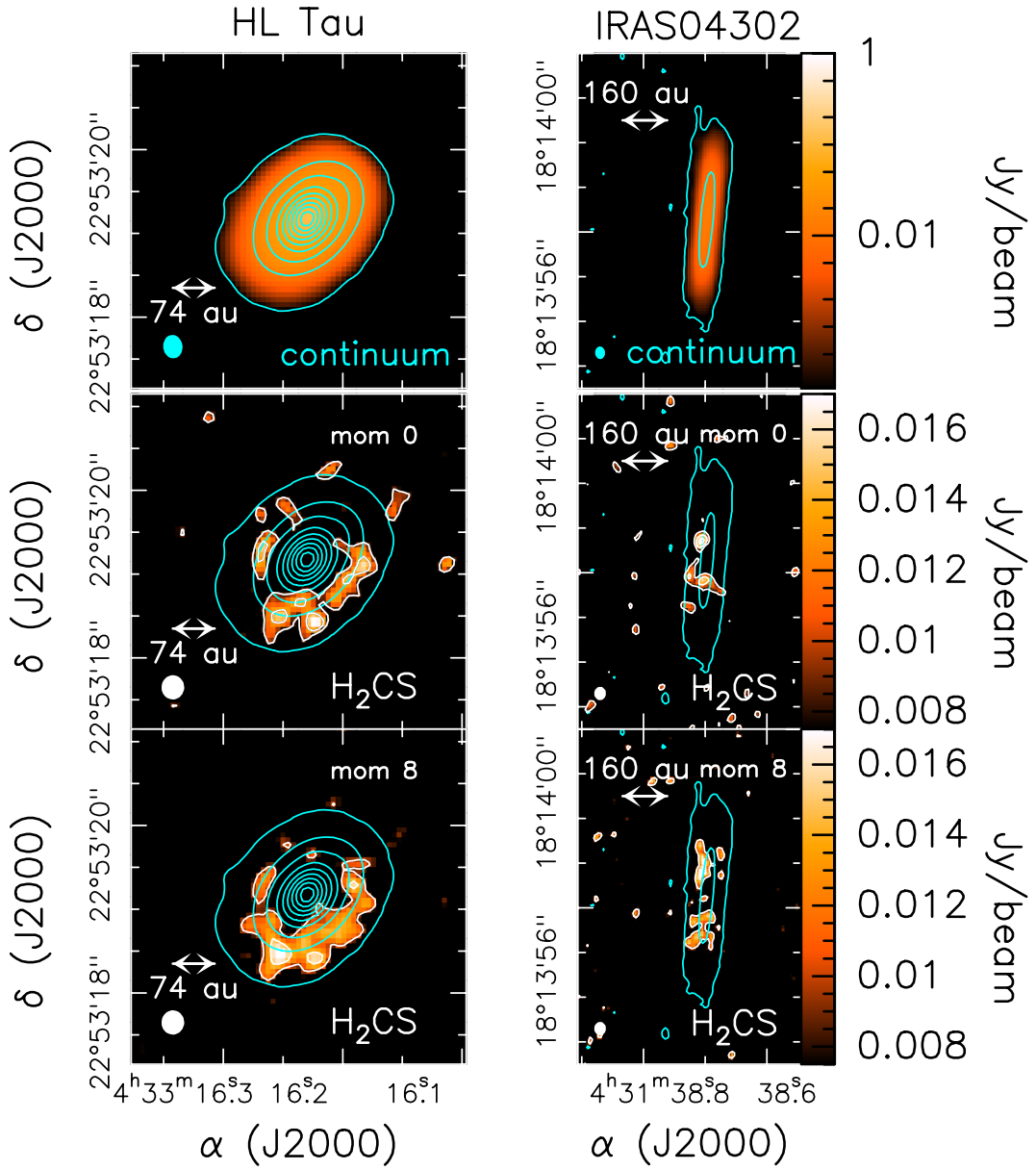


Fig. 1. *Upper panels*: map (cyan contours and colour scale) of the 1.3 mm dust continuum distribution for HL Tau (*left*) and IRAS 04302+2247 (*right*) discs. First contours and steps are 3σ (200 μJy beam^{-1}, HL Tau; 115 μJy beam^{-1}, IRAS 04302+2247), and 200σ, respectively. The ellipse in the bottom-left corner shows the ALMA synthesised beam (HPBW): $0\farcs28 \times 0\farcs25$ (PA = –7°), for HL Tau, and $0\farcs28 \times 0\farcs22$ (PA = –3°), for IRAS 04302+2247. *Middle panels*: spatial distribution (moment 0) maps (white contours and colour scale) of the o-$H_2CS(7_{1,6}–6_{1,5})$ line based on the velocity integrated emission (3–11 km s^{-1}, HL Tau, 2–10 km s^{-1}, IRAS 04302+2247) overlaid on the continuum maps (cyan contours). First contours and steps are 5σ (7.5 mJy beam^{-1} km s^{-1}, HL Tau, and 12.5 mJy beam^{-1} km s^{-1}, IRAS 04302), and 3σ, respectively. The ellipse shows the synthesised beam (HPBW): $0\farcs29 \times 0\farcs27$ (PA = 2°) for HL Tau and $0\farcs30 \times 0\farcs26$ (PA = 2°) for IRAS 04302+2247. *Lower panels*: moment 8 maps (white contours and colour scale) of the $H_2CS(7_{1,6}–6_{1,5})$ based on the same velocity integrated emission used for the moment 0 maps, overlaid on the continuum maps (cyan contours). First contours and steps are 5σ (3 mJy beam^{-1} km s^{-1}), and 3σ, respectively.

IRAS 04302+2247 (herafter IRAS 04302). For DG Tau, DG Tau B, and Haro 6–13, upper limits on H_2CS emission are reported in the following sections. As a reference to analyse molecular emission, Fig. 1 (upper panels) reports the dust continuum emission. The well-known HL Tau disc (d = 147 pc; Galli et al. 2018), with an inclination angle i of 47° (e.g. ALMA Partnership 2015; Carrasco-González et al. 2019), is well traced, showing a radius of ∼150 au. The dust continuum at 227 GHz peaks (118 mJy beam^{-1}) at α(J2000) = $04^h31^m38\fs44$, δ(J2000) = +18°13′57.″65. On the other hand, the IRAS 04302 disc (Guilloteau et al. 2013; Podio et al. 2020a), located at d = 161 pc (Galli et al. 2019), is more extended (∼350 au), and is associated with an almost edge-on geometry, $i \sim 90°$ (Wolf et al. 2003). The coordinates of the continuum peak, 133 mJy beam^{-1}, are α(J2000) = $04^h33^m16\fs47$, δ(J2000) = +22°53′20.″36.

Figure 1 (middle) also reports the intensity integrated maps (moment 0) of the o-$H_2CS(7_{1,6}–6_{1,5})$ emission as observed towards HL Tau and IRAS 04302, thus providing for the first time the thioformaldeyde radial (HL Tau) and vertical (IRAS 04302) distributions. All the channels showing emission of at least 3σ (see Sect. 2) have been used, namely: 3–11 km s^{-1} (HL Tau) and 2–10 km s^{-1} (IRAS 04302). The signal-to-noise

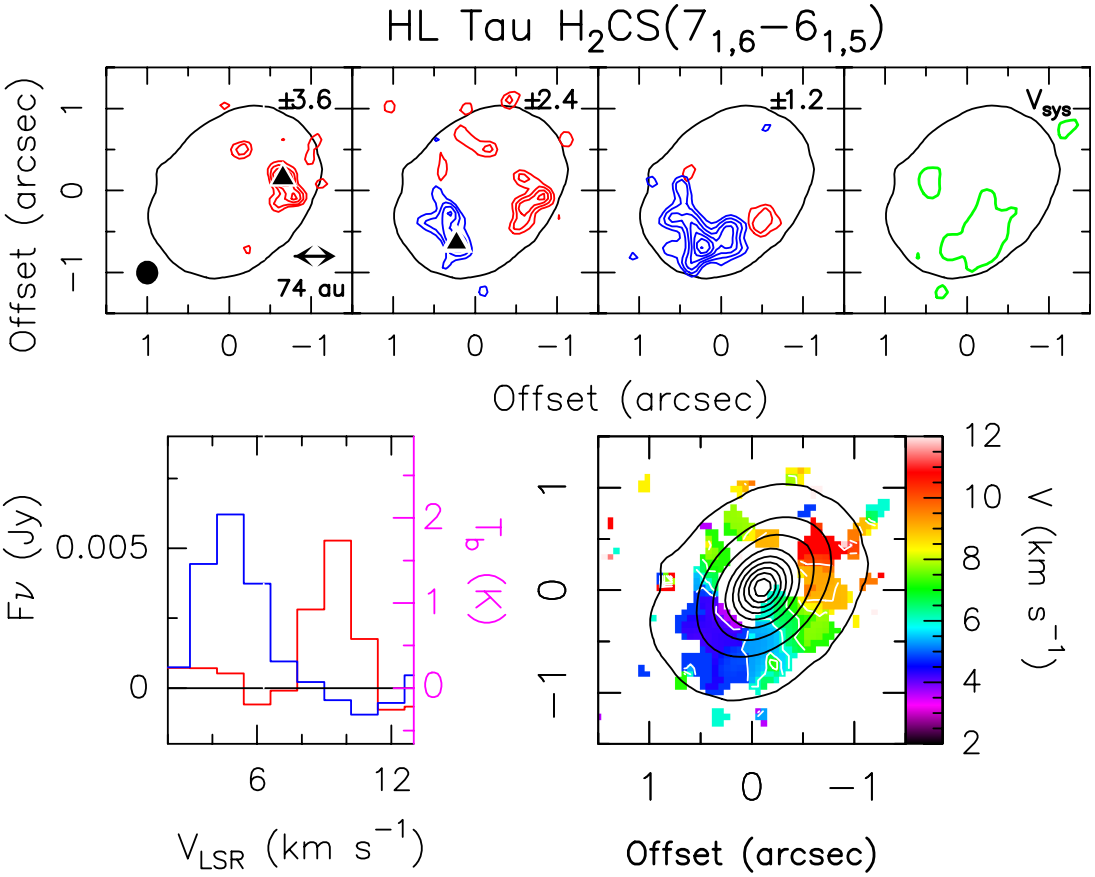


Fig. 2. *Upper panels*: channel maps of the o-$H_2CS(71, 6–61, 5)$ blue- and redshifted emission in the HL Tau disc. Each panel shows the emission integrated over a velocity interval of 1.2 km s^{-1} shifted with respect to the systemic velocity (~+7 km s^{-1}, green) by the value given in the upper-right corner. We report the 3σ contour of the continuum emission in black (Fig. 1). The black triangles indicate where spectra have been extracted. The ellipse shows the synthesised beam (HPBW): 0.″29 × 0.″27 (PA = 2°). First contours and steps correspond to 3σ (2.1 mJy beam^{-1}) and 1σ, respectively. Offsets are derived with respect to the continuum peak. *Bottom left panel*: o-$H_2CS(71, 6–61, 5)$ spectra in flux and brightness temperature scales ($T_b/F_\nu = 328.593$) extracted in the positions marked with a red or blue triangle in the upper panels. *Bottom right panel*: first-moment map in colour scale.

ratio (S/N) of the velocity integrated emission is greater than 8 in both sources. For HL Tau, the image clearly shows an H_2CS ring around a central dip. The outer radius is about 140 pc, while the dip is confined in the inner ~35 au. For IRAS 04302, the picture provided by the moment 0 map is less clear. The H_2CS emission is confined to the inner 0.″7, ~115 au. In Sect. 3, we show how kinematics lead us to infer the structure of the emitting region.

Finally, the bottom panels of Fig. 1 report the HL Tau and IRAS 04302 $H_2CS(7_{1,6}–6_{1,5})$ spatial distributions of the peak intensity in colour scale, as derived using the moment 8 method[4] to improve the images. The moment 8 CASA algorithm was used, collapsing the intensity axis of the ALMA datacube to one pixel and setting the value of that pixel (for RA and Dec) to the maximum value of the spectrum. The moment 8 images confirm the finding from the moment 0 maps. In Sect. 5.2, the spatial distribution is compared with those of other molecular species.

3.2. H_2CS kinematics

Figures 2 and 3 summarise the kinematics of HL Tau and IRAS 04302 provided by: (i) channel maps, (ii) intensity-weighted mean velocity (moment 1) maps, and (iii) H_2CS spectra as extracted towards the brightest positions. The H_2CS in HL Tau is clearly rotating with the blue- and redshifted sides located towards the SE and NW, respectively. The systemic velocity is ~+7.0 km s^{-1} (in agreement with ALMA Partnership 2015; Wu et al. 2018). The same rotating gradient has been observed using HCO^+ (ALMA Partnership 2015; Yen et al. 2019), $C^{18}O$ (Wu et al. 2018), and $^{13}C^{17}O$ (Booth & Ilee 2020). Also the emission towards the disc of IRAS 04302 shows a rotation pattern. Its almost edge-on orientation allows us to clearly disentangle the red- (southern) and blueshifted (northern) lobes. The systemic velocity estimated from the velocity distribution of the bright H_2CO line is +5.6 km s^{-1} (Podio et al. 2020a), in good agreement with IRAM 30-m CN, H_2CO, CS, and $C^{17}O$ spectra of Guilloteau et al. (2013, 2016). The rotation pattern has been imaged also by Podio et al. (2020a), who found, using CO, H_2CO, and CS emission, a molecular emission which is vertically stratified (see Sect. 4 for the comparison with H_2CS).

The H_2CS channel maps show that the emission shifted by less than 2 km s^{-1} is emitted from the inner 0.″5 region, whereas at larger velocities we detect emission up to 1.″2 from the protostar. This suggests that larger projected velocities (in particular the blueshifted velocity) have a larger projected positional offset from the protostar. In other words, the present dataset suggests that $V \propto R$. This is the standard signature of a rotating ring with an inner dip, and not a filled disc for which we would see the

[4] https://casa.nrao.edu/Release3.4.0/docs/UserMan/UserManse41.html

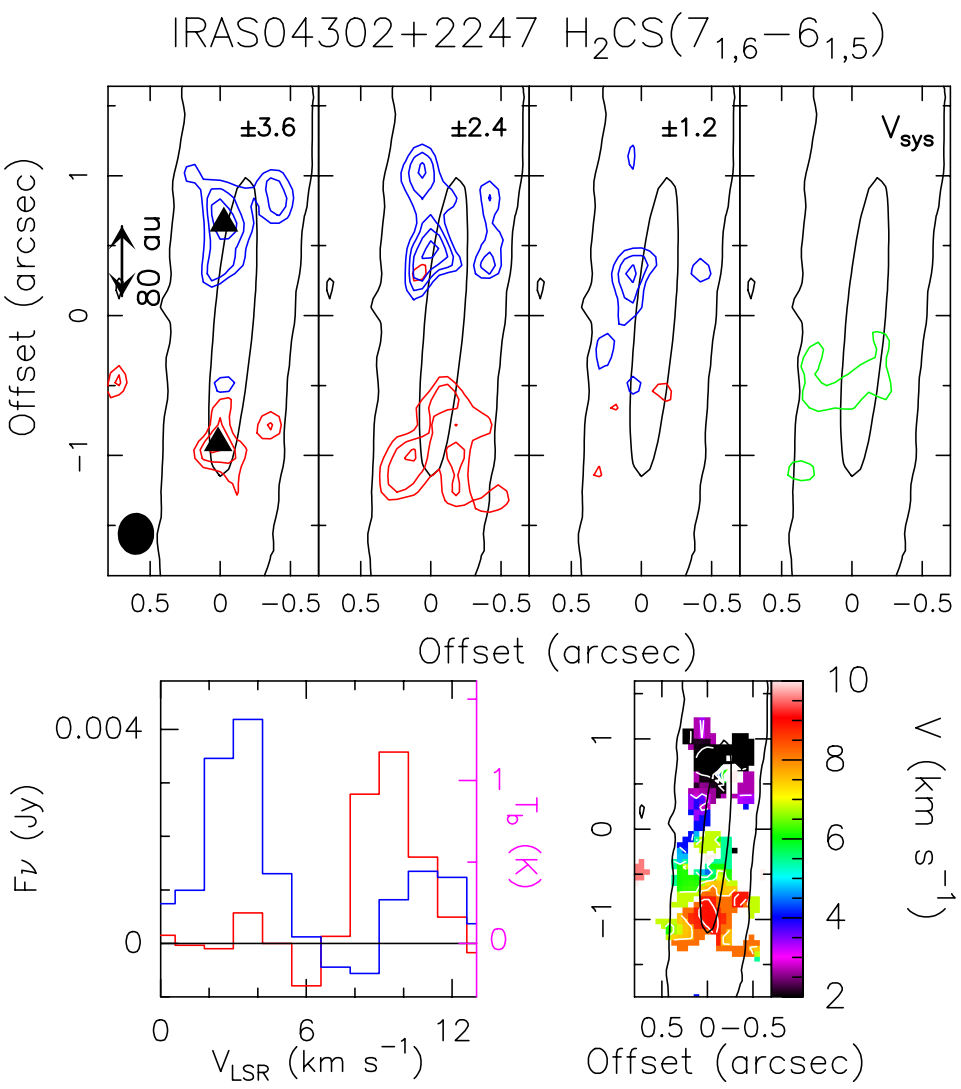


Fig. 3. *Upper panel*: channel maps of the o-$H_2CS(7_{1,6}$–$6_{1,5})$ blue- and redshifted emission in the IRAS 04302+2247 disc. Each panel shows the emission integrated over a velocity interval of 1.2 km s^{-1} shifted with respect to the systemic velocity (∼+5.6 km s^{-1} Podio et al. 2020a, green) by the value given in the upper-right corner. We report the 3σ contour of the continuum emission in black (Fig. 1). The black triangles indicate where spectra have been extracted. The ellipse shows the synthesised beam (HPBW): 0.″30 × 0.″26 (PA = 2°). First contours and steps correspond to 3σ (2.1 mJy beam^{-1}) and 1σ, respectively. Offsets are derived with respect to the continuum peak. *Bottom left panel:* o-$H_2CS(7_{1,6}$–$6_{1,5})$ spectra in flux and brightness temperature scales ($T_b/F_\nu = 328.593$) extracted in the positions marked with a red or blue triangle in the upper panels. *Bottom right panel*: first-moment map in colour scale.

opposite trend, with $V \propto R^{-2}$. Very recently, Oya & Yamamoto (2020) reported the detection of H_2CS in the IRAS16293 A protostellar disc (see also van 't Hoff et al. 2020). In addition, the present findings closely resemble what was found for the archetypical protostellar disc HH212, which is also close to being edge-on as in IRAS 04302 (e.g. Lee et al. 2019, and references therein). Also in this case, a chemical enrichment in the gas phase associated with rotating rings is revealed by the $V \propto R$ kinematical feature (see e.g. the recent review by Codella et al. 2019).

3.3. H_2CS column densities and abundances

Assuming (i) local thermodynamic equilibrium (LTE) and (ii) optically thin emission, the column densities of the H_2CS are derived. The first assumption is well justified as the H_2 gas density in the molecular layers is larger than 10^7 cm^{-3} (see e.g. Walsh et al. 2014; Le Gal et al. 2019), i.e. well above the critical density of the considered o-$H_2CS(7_{1,6}$–$6_{1,5})$ line (n_{cr} ∼ a few 10^4 cm^{-3}) in the 20–150 K range[5]. The second assumption is justified as models indicate an abundance (with respect to H) of H_2CS lower than 10^{-10} (Le Gal et al. 2019; Loomis et al. 2020).

In HL Tau, the observed emitting area is 1.35 arcsec^2 (from the moment 0 map) and the flux is 148 mJy km s^{-1} (2.6 K km s^{-1}). Le Gal et al. (2019) estimated an H_2CS rotational temperature between 20 and 80 K in the MWC 480 disc. We conservatively adopted a temperature between 20 and 150 K. An ortho-to-para ratio of 3, i.e. the statistical value, was assumed (as done by Le Gal et al. 2019). We find a total H_2CS column density N_{H_2CS} (averaged on the emitting area) of 0.9–1.4 × 10^{14} cm^{-2}. For IRAS 04302 the emitting area is smaller with respect to HL Tau, namely 0.72 arcsec^2, and the flux is ≃78 mJy km s^{-1} (2.5 K km s^{-1}). The column density N_{H_2CS} is, similarly to

[5] Using scaled H_2CO collisional rates from Wiesenfeld & Faure (2013), see Schöier et al. (2005).

HL Tau, $\simeq 10^{14}$ cm^{-2}. These values can also be considered as an a posteriori check that the observed H_2CS emission is optically thin. Indeed, by assuming kinetic temperatures larger than 20 K and densities larger than 10^7 cm^{-3}, the large velocity gradient approach confirms that column densities around 10^{14} cm^{-2} imply an opacity of $\leq$0.1 for the o-$H_2CS(7_{1,6}$–$6_{1,5})$ line. These column density estimates are a factor 30 higher than those measured by Le Gal et al. (2019) and Loomis et al. (2020) towards the massive disc MWC 480 (3×10^{12} cm^{-2}). However, as reported by the authors, their spatial resolution is not high enough to evaluate the presence of a central dip, which could cause an underestimate the H_2CS column density.

For HL Tau, a further step can be taken given that Booth & Ilee (2020) published an ALMA map of the $^{13}C^{17}O(3$–$2)$ emission at a similar angular scale to that of our H_2CS maps. The $^{13}C^{17}O$ spatial distribution agrees well with that of H_2CS. The emission is considered optically thin, given that its abundance ratio with respect to $^{12}C^{16}O$ is 8.3×10^{-6} (Milam et al. 2005). Taking the $^{13}C^{17}O$ flux density of 10–20 mJy beam^{-1} km s^{-1}, and an excitation temperature, as for H_2CS, in the 20–150 K range, we derive $N_{CO} \simeq 5$–10×10^{23} cm^{-2}. Using [CO]/[H] $= 5 \times 10^{-5}$, we find a H_2CS abundance (with respect to H) of $X(H_2CS) \simeq 10^{-14}$. A comparison with the H_2CS abundances predicted by disc chemistry is challenging, given that this latter depends significantly on the initial composition of the S-species, which can vary by orders of magnitude (see e.g. Fedele & Favre 2020). Vice versa, the present measured H_2CS abundances will hopefully be used in future chemical models to constrain their initial conditions.

Finally, the upper limits on the H_2CS column densities in DG Tau, DG Tau B, and Haro 6-13, derived taking the 5σ level of the moment 0 maps and using all the assumptions described above, are: $N_{H_2CS} \leq 2 \times 10^{13}$ cm^{-2} (DG Tau B) and $N_{H_2CS} \leq 4 \times 10^{13}$ cm^{-2} (DG Tau and Haro 6-13).

4. Binding energies: ice modelling and computational methods

We computed the H_2CS and CS BEs, adopting a proton-ordered (P-ice) crystalline model (Casassa et al. 1997) for the bulk ice. The ice surface where the adsorption takes place was simulated by a finite slab model of the (010) surface cut out from the bulk P-ice crystal, as recently proposed by Ferrero et al. (2020) to predict the BEs of a set of 21 molecules using the periodic ab initio program CRYSTAL17 (Dovesi et al. 2018). CRYSTAL17 adopts localised (Gaussian) basis functions that allow the surfaces to be simulated as true 2D systems, without including fake replicas of the slab separated by artificial voids. The surface slab model is sufficiently thick (number of water layers) to ensure a converged surface energy (energy penalty to cut the surface from the bulk ice). The choice of a crystalline ice model goes against the overwhelming evidence that ice in the interstellar environment is amorphous in nature (AWS). There are two main reasons that hinder the adoption of an AWS phase at the modelling level: (i) the experimental atomistic structure of the AWS is unknown; and (ii) any AWS model should be based on a very large unit cell to mimic the disordered nature of the ice. Point (i) means that the model cannot be derived from experimental evidence and therefore any model is somehow arbitrary. Point (ii) implies that very expensive calculations are needed to cope with the large unit cells. In the following, we propose a simplified strategy to derive the values of the BEs for the H_2CS and CS molecules as adsorbed on AWS, without the need to run expensive calculations, but taking advantage of the results of Ferrero et al. (2020) on the analogous CO and H_2CO molecules, in which both crystalline and AWS models were studied.

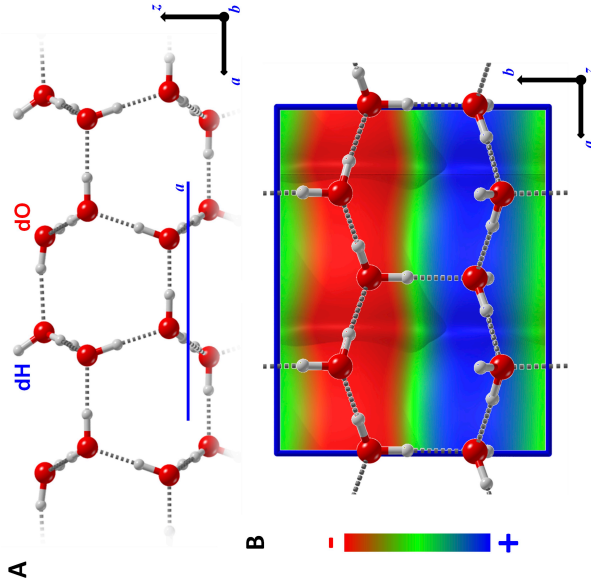


Fig. 4. HF-3c optimised P-ice slab model. The adsorption crystallographic plane is the Miller (010) one. *Panel A*: side view along the *b* lattice vector. *Panel B*: top view of the 2×1 supercell ($|a| = 9.065$ Å and $|b| = 7.154$ Å) along with its ESP map. Colour code: +0.02 atomic unit (blue, positive), 0.00 atomic unit (green, neutral) and –0.02 atomic unit (red, negative).

First, we set up the starting locations of H_2CS and CS molecules at the ice surface using the optimised positions of the analogous CO and H_2CO molecules after Ferrero et al. (2020) and then fully optimising the structures. We choose the HF-3c method, which combines the Hartree-Fock Hamiltonian with the minimal basis set MINI-1 (Tatewaki & Huzinaga 1980) supplemented by three a posteriori corrections for: (i) the basis set superposition error (BSSE) arising when localised Gaussian functions are used to expand the basis set (Jansen & Ros 1969; Liu & McLean 1973); (ii) the dispersive interactions; and (iii) short-ranged deficiencies due to the adopted minimal basis set (Sure & Grimme 2013). The resulting optimised unit cell of the ice (010) surface is shown in Fig. 4, together with the mapping of the electrostatic potential (ESP) computed at HF-3c level of theory. The ESP reveals the oxygen-rich (red color, ESP < 0) and proton-rich (blue color, ESP > 0) regions, acting as, respectively, H-bond acceptors and donors with respect to specific adsorbates.

In order to get accurate BEs, the HF-3c structures were used to compute single-point energy evaluations at B3LYP-D3(BJ) level of theory (Becke 1993). A dispersion interaction is included through the D3 correction, with the Becke-Johnson damping scheme (Grimme et al. 2010). The Ahlrichs' triple-zeta quality VTZ basis set supplemented with a double set of polarization functions (Schäfer et al. 1992) was adopted to define the final B3LYP-D3(BJ)/A-VTZ*//HF-3c model chemistry. BEs were also corrected for BSSE.

For H_2CS, the most stable structure shows a symmetric involvement of the CH_2S molecule with the ice surface, in which the C-H bonds act as weak H-donors toward the surface oxygen atoms, while the S atom acts as a H-bond acceptor at the dangling surface OH groups. For CS, the adsorption occurs through the C-end with a very long H-bond with the dangling ice OH group. Any attempt to engage the CS molecule through the

Table 1. H_2CS and CS BEs (Kelvin) derived for the crystalline (CRY) and amorphous (AWS) ice models.

	BE-CRY	BE-AWS	Das [(a)]	Wakelam [(b)]
H_2CS	4258	3000–4600	3110	4400
CS	3861	2700–4000	2217	3200

Notes. See the text for the procedure adopted to obtain the BE-AWS values.
References. [(a)]Das et al. (2018); [(b)]Wakelam et al. (2017).

S-end of the molecule evolved spontaneously to the C-end one. Obviously, the relatively simple structure of the crystalline P-ice does not allow us to explore alternative configurations to those described, at variance with the results for an AWS model which would be expected to provide many times more adsorption sites of different strength. Furthermore, due to the long range order of the water molecules in the crystalline ice, the H-bond interactions will cooperate to enhance the H-bond donor(acceptor) character of the surface water molecules, giving very high(low) values of the ESP (see Fig. 4). This means that the BEs resulting from the crystalline model should be taken as an upper limit, as shown by Ferrero et al. (2020). As anticipated, to mitigate the deficiencies of the crystalline ice model we resort to data from the work by Ferrero et al. (2020) for the analogous CO and H_2CO molecules (with respect to CS and H_2CS treated here) adsorbed on the AWS model. As expected, these latter authors found a relatively complex adsorption scenario at AWS in comparison to that occurring at the P-ice surface. For CO, five different adsorption sites have been characterised; for H_2CO, up to eight different adsorption sites were predicted. Obviously, each of these adsorption sites provides different values of the BE and in the limit of very large AWS models, the BE values will obey a certain distribution. It is clear that a similar study should be carried out for CS and H_2CS, but instead, as anticipated, we resort to a simplified scheme to estimate the BE values for the AWS, without actually running any calculation.

First, from the data by Ferrero et al. (2020), we worked out two scaling factors (0.859 and 0.775, respectively) connecting the BE of the CO and H_2CO analogues computed for the P-ice to their corresponding averaged BE values for the AWS model. Subsequently, by assuming the same scaling factors for the present CS and H_2CS cases, we scaled the BEs for the crystalline ice to estimate their averaged values on the AWS model. In agreement with the CO and H_2CO cases, the BE-AWS for CS and H_2CS are smaller than those for the crystalline ice. Table 1 reports the derived BEs on crystalline (H_2CS: 4258 K; CS: 3861 K) and AWS (H_2CS: 3000-4600 K; CS: 2700–4000 K) ice for both H_2CS and CS.

5. Discussion

5.1. Comparison with previous BE measurements

Interstellar molecules are formed either through gas-phase reactions or directly on grain surfaces. Regardless of the formation route, gaseous molecules freeze out into the grain mantles on timescales that depend on the density and temperature of the gas and dust as well as the molecule BE. Thus, in cold and dense regions, as in the outer disc regions and in the layers close to the disc midplane, icy mantles envelope the dust grains. The frozen molecules can then be injected into the gas phase via three processes (see e.g. Walsh et al. 2014): (i) thermal desorption, (ii) UV-photodesorption and/or CR-induced desorption, and (iii) reactive desorption. The first process occurs inside the so-called snow lines, which is the location where the dust temperature is high enough to allow the species to sublimate.

Regarding H_2CO, its BE has been experimentally measured on amorphous water surface (AWS) through a thermal desorption process by Noble et al. (2012), for example, to be 3260 ± 60 K, and was also estimated via theoretical computations on AWS and crystalline ice models by Ferrero et al. (2020), who found zero-point-corrected BEs (see Sect. 4) in the 3071–6194 K range for the AWS case, therefore bracketing the experimental value. The BE for the crystalline ice falls at 5187 K, in the higher regime of the AWS range.

Following the described procedure, for H_2CS we find BE values of 4258 and 3000–4600 K for the crystalline and AWS ice models, respectively. For CS, we find slightly lower values: 3861 K (crystalline) and 2700–4000 K (AWS). Table 1 compares our results with the available literature data, all coming from computer simulations. The BEs computed by Das et al. (2018), who adopted a tetramer of water molecules to simulate the ice, are at the lower end of our computed BEs range, whereas the BE computed by Wakelam et al. (2017) based on one single water molecule and corrected with an empirical factor, lies at the higher end of our range.

Based on the new computations that we present in Sect. 4 and using a BE ranging from 3000 to 4600 K, H_2CS is expected to thermally sublimate in regions of the disc where the dust temperature exceeds ~50 to ~80 K, respectively. We emphasise that the dispersion in our computed BEs reflects the different possible sites of adsorption of H_2CS, and it is therefore physical and not due to a computational uncertainty (see the discussion in Ferrero et al. 2020). Although we cannot a priori say how many sites are populated with each different BE, we can conservatively assume that H_2CS molecules should remain frozen in regions of the disc with dust temperatures lower than 50–80 K. The fact that H_2CS emission is seen up to outer radii of ~140 au (HL Tau) and ~115 au (IRAS 04302) suggests that non-thermal processes are likely responsible for the presence of H_2CS in the gas in those disc regions.

5.2. Comparison between H_2CS, CS, and H_2CO

The formation routes of H_2CS were recently summarised by Le Gal et al. (2019), who used the gas–grain chemical model Nautilus (Wakelam et al. 2016) supported by the gas chemical dataset KIDA (Wakelam et al. 2015), and by Fedele & Favre (2020), who adopted the thermo-chemical model DALI (Bruderer et al. 2012) coupled with the chemical network UMIST (Woodall et al. 2007). Generally, H_2CS is mainly (99%) formed in the gas phase via neutral-neutral reaction of atomic S with CH_3. On the other hand, CS in discs is also thought to be mainly formed in the gas phase, through reactions starting with small hydrocarbons interacting with S^+ (in upper disc layers) or S (in inner slabs). Finally, H_2CO can be formed on grains due to hydrogenation processes as well and in the gas phase by oxygen reacting with CH_3, in an analogous way to $S + CH_3 \rightarrow H_2CS$ (see e.g. Fedele & Favre 2020, and references therein).

For the IRAS 04302 disc, the H_2CS vertical intensity profile can be compared with those of CS and formaldehyde (H_2CO); see Podio et al. (2020a). To this end, we averaged the emission radially over 3 pixels (0.″18, corresponding to ~29 au) around the selected radius. Figure 5 shows a comparison obtained at 60 and 115 au from the protostar. We note that the H_2CS intensity has been multiplied by the factor reported in the labels in order to

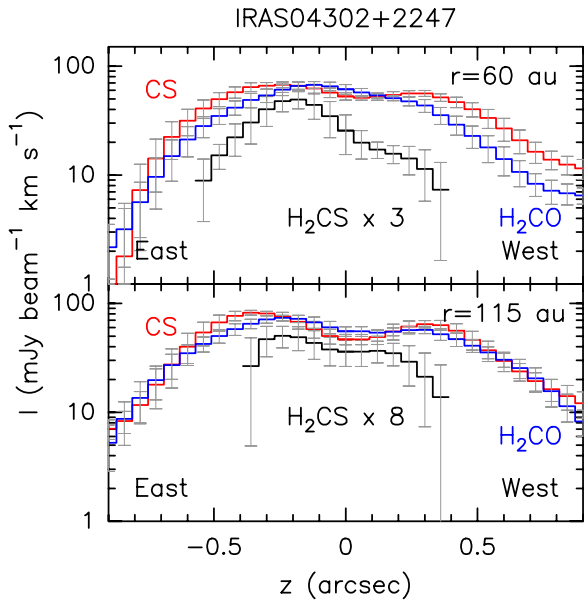


Fig. 5. Vertical intensity profile z of H_2CS (black) compared with those of CS(5–4) (red) and o-$H_2CO(3_{1,2}–2_{1,1})$ (blue), from Podio et al. (2020a). Only fluxes above 3σ confidence are shown. The H_2CS intensity has been scaled in order to better compare its profile with those of o-H_2CO and CS. The inner 1.″8 region is shown, with the positive (negative) values sampling the eastern (western) side. The angular resolution is 0.″25 (40 au). The profiles are obtained at ~60 au (*upper panel*) and 115 au (*lower panel*) from the protostar.

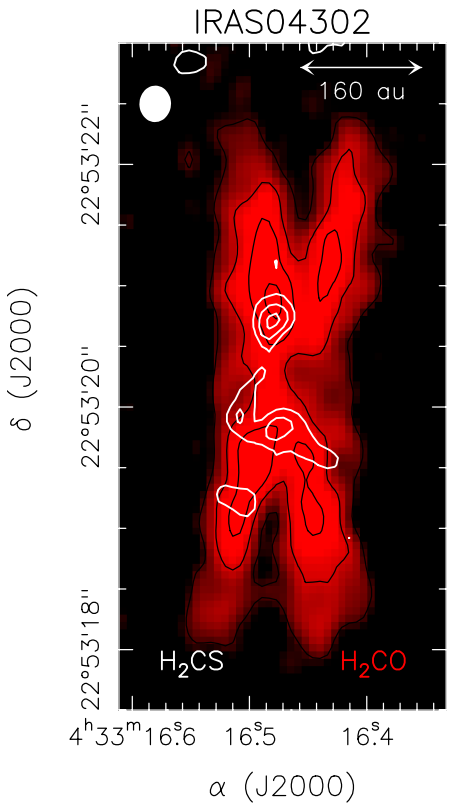


Fig. 6. Spatial distribution (moment 0) maps (white contours) of the o-$H_2CS(7_{1,6}–6_{1,5})$ line (see Fig. 1) overlaid on the o-$H_2CO(3_{1,2}–2_{1,1})$ reported by Podio et al. (2020a), in black contours and red scale. Symbols are as in Fig. 1.

better compare with those of o-H_2CO and CS. The vertical distribution of H_2CS (black) shows an asymmetry with respect to the disc midplane (i.e. $z = 0$), with the emission from the eastern disc side being brighter than in the western side by a factor 1.8 at 60 au radial distance and a factor 1.5 at 115 au. The same asymmetry in the vertical distribution is observed in the H_2CO (blue) and CS (red) emission, and all three species peak at a disc height, z, of about 50 au. This suggests that, at our resolution, the emission from H_2CS, H_2CO, and CS originates from the same disc layer. As discussed by Podio et al. (2020a), the bulk of the H_2CO and CS emission originates from the disc molecular layer where molecules are either released from dust grains orare formed in the gas phase. Given that H_2CS is co-spatial with H_2CO and CS and that all three molecules can be efficiently formed in the gas phase using small hydrocarbons (e.g. CH_3), we suggest that H_2CS may form in similar way.

The comparison between the moment 0 distributions of H_2CS and H_2CO (Podio et al. 2020a) is also instructive (see Fig. 6), revealing slightly different radial distributions of the two molecules. The H_2CO (and CS) emission extends radially out to ~480 au and peaks at ~120 au, while the H_2CS emission is radially confined in the inner 115 au with a peak at ~70 au. The radial distribution of H_2CS suggests that the o-$H_2CS(7_{1,6}–6_{1,5})$ line probes an inner portion of the IRAS 04302 disc, possibly due to a higher E_{up} (of 60 K) with respect to those of the o-$H_2CO(3_{1,2}–2_{1,1})$ and CS(5–4) (of 33–35 K). Only further observations of a species using different excitation lines will shed light on this hypothesis.

6. Conclusions

We present the first images of the radial (HL Tau) and vertical (IRAS 04302) spatial distribution of the o-H_2CS emission as observed towards Class I protoplanetary discs using ALMA on a Solar System scale. These observations were performed in the context of the ALMA chemical survey of Disk-Outflow sources in the Taurus star forming region (ALMA-DOT). H_2CS is confined to a rotating ring with an inner dip towards the protostar: the outer radii are 140 au (HL Tau) and 115 au (IRAS 04302). The edge-on geometry of IRAS 04302 allows us to reveal that H_2CS emission peaks at $r = 60$–115 au, which is at $z = \pm 50$ au from the equatorial plane. Assuming LTE conditions, the column densities are $\sim 10^{14}$ cm^{-2}. For HL Tau, we derived, for the first time, the [H_2CS]/[H] abundance in a protoplanetary disc ($\simeq 10^{-14}$). The o-$H_2CS(7_{1,6}–6_{1,5})$ line emits where the emission of CS(5–4) and o-$H_2CO(3_{1,2}–2_{1,1})$ is brighter (Podio et al. 2020a), that is, the so-called warm molecular layer. H_2CS emission peaks closer to the protostar with respect to H_2CO and CS, possibly because of the higher energy of the upper level (60 K) of the observed transition with respect to those of H_2CO and CS (33–35 K), which requires higher gas temperature, hence favouring the emission from the inner disc regions.

The present work also provides the H_2CS and CS BEs as computed for the first time for an extended crystalline ice (4258 K for H_2CS, and 3861 K for CS) and estimated for an AWS model using recipes from previous studies (Ferrero et al. 2020) to be in the 3000–4600 K and 2700–4000 K ranges, respectively. In turn, for ~1 $L_\odot$ protostars, this implies that radially thermal desorption rules in an inner region, while vertically only a thin upper layer is sufficiently hot (see e.g. Walsh et al. 2014; Le Gal et al. 2019). In conclusion, the observed H_2CS, and more precisely that detected at radii up to more than 100 au, is likely released into the gas because of non-thermal processes (photodesorption, CR-induced desorption, and/or reactive-desorption).

Acknowledgements. We thank the anonymous referee for instructive discussion and suggestions. This paper uses the ADS/JAO.ALMA 2016.1.00846.S and ADS/JAO.ALMA 2018.1.01037.S (PI: L. Podio) ALMA data. ALMA is a partnership of ESO (representing its member states), NSF (USA) and NINS (Japan), together with NRC (Canada), MOST and ASIAA (Taiwan), and KASI (Republic of Korea), in cooperation with the Republic of Chile. This work was supported by the European Research Council (ERC) under the European Union's Horizon 2020 research and innovation programmes: (i) "The Dawn of Organic Chemistry" (DOC), grant agreement No 741002, and (ii) "Astro-Chemistry Origins" (ACO), Grant No 811312. C.F. acknowledges financial support from the French National Research Agency in the framework of the Investissements d'Avenir program (ANR-15-IDEX-02), through the funding of the "Origin of Life" project of the Univ. Grenoble-Alpes. D.F. acknowledges financial support from the Italian Ministry of Education, Universities and Research, project SIR (RBSI14ZRHR).

References

ALMA Partnership (Brogan, C. L., et al.) 2015, ApJ, 808, L3
Anders, E., & Grevesse, N. 1989, Geochim. Cosmochim. Acta, 53, 197
Andre, P., Ward-Thompson, D., & Barsony, M. 2000, Protostars & Planets IV (Tucson, AZ: University of Arizona Press)
Andrews, S. M., Huang, J., Pérez, L. M., et al. 2018, ApJ, 869, L41
Becke, A. D. 1993, J. Chem. Phys., 98, 1372
Belloche, A., Maury, A. J., Maret, S., et al. 2020, A&A, 635, A198
Bianchi, E., Chandler, C. J.. Ceccarelli, C., et al. 2020, MNRAS, 498, L87
Boogert, A. C. A., Gerakines, P. A., & Whittet, D. C. B. 2015, Ann. Rev., 53, 541
Booth, A. S., & Ilee, J. D. 2020, MNRAS, 493, L108
Booth, A. S., Walsh, C., Kama, M., et al. 2018, A&A, 611, A16
Bruderer, S., van Dishoeck, E. F., Doty, S. D., & Herczeg, G. J. 2012, A&A, 541, A91
Carrasco-González, C., Sierra, A., Flock, M., et al. 2019, ApJ, 883, 71
Casassa, S., Ugliengo, P., & Pisani, C. 1997, J. Chem. Phys., 106, 8030
Caselli, P., & Ceccarelli, C. 2012, A&ARv, 20, 56
Ceccarelli, C., Caselli, P., Herbst, E., Tielens, A. G. G. M., & Caux, E. 2007, Protostars and Planets V, eds. B. Reipurth, D. Jewitt, & K. Keil (Tucson, AZ: University of Arizona Press), 47
Ceccarelli, C., Caselli, P., Fontani, F., et al. 2017, ApJ, 850, 176
Codella, C., Bachiller, R., Benedettini, M., et al. 2005, MNRAS, 361, 244
Codella, C., Ceccarelli, C., Lee, C.-F., et al. 2019, ACS Earth Space Chem., 3, 2110
Das, A., Sil, M., Gorai, P., Chakrabarti, S. i. K., & Loison, J. C. 2018, ApJS, 237, 9
Dovesi, R., Orlando, R., Erba, A., et al. 2018, Wiley Interdiscip. Rev. Comput. Mol. Sci., 176
Dutrey, A., Guilloteau, S., & Guelin, M. 1997, A&A, 317, L55
Dutrey, A., Guilloteau, S., Piétu, V., et al. 2017, A&A, 607, A130
Favre, C., Bergin, E. A., Cleeves, L. I., et al. 2015, ApJ, 802, L23
Favre, C., Fedele, D., Semenov, D., et al. 2018, ApJ, 862, L2
Favre, C., Fedele, D., Maud, L., et al. 2019, ApJ, 871, 107
Fedele, D., & Favre, C. 2020, A&A, 638, A110
Fedele, D., Carney, M., Hogerheijde, M. R., et al. 2017, A&A, 600, A72
Fedele, D., Tazzari, M., Booth, R., et al. 2018, A&A, 610, A24
Ferrero, S., Zamirri, R., Ceccarelli, C., et al. 2020, ApJ, 904, 11,
Fuente, A., Cernicharo, J., Agúndez, M., et al. 2010, A&A, 524, A19
Galli, P. A. B., Loinard, L., Ortiz-Léon, G. N., et al. 2018, ApJ, 859, 33
Galli, P. A. B., Loinard, L., Bouy, H., et al. 2019, A&A, 630, A137
Garufi, A., Podio, L., Codella, C., et al. 2020, A&A 636, A65
Grimme, S., Antony, J., Ehrlich, S., & Krieg, H. 2010, J. Chem. Phys., 132, 154104
Guilloteau, S., Di Folco, E., Dutrey, A., et al. 2013, A&A, 549, A92
Guilloteau, S., Simon, M., Piétu, V., et al. 2014, A&A, 567, A117
Guilloteau, S., Reboussin, L., Dutrey, A., et al. 2016, A&A, 592, A124
Herbst, E., & van Dishoeck, E. F. 2009, ARA&A, 47, 427
Holdship, J., Viti, S., Jimenez-Serra, I., et al. 2016, MNRAS, 463, 802
Jansen, H., & Ros, P. 1969, Chem. Phys. Lett., 3, 140
Jørgensen, J. K., van der Wiel, M. H. D., Coutens, A., et al. 2016, A&A, 595, A117
Laas, J. C., & Caselli, P. 2019, A&A, 624, A108
Lee, C.-F., Li, Z.-Y., & Turner, N. J. 2019, Nat. Astron., 466, 24
Lefloch, B., Bachiller, R., Ceccarelli, C., et al. 2018, MNRAS, 477, 4792
Le Gal, R., Öberg, K. I., Loomis, R. A., Pegues, J., & Bergner, J. B. 2019, ApJ, 876, 72
Le Gal, R., Öberg, K. I., Huang, J., et al. 2020, ApJ, 898, 131
Liu, B., & McLean, A. D. 1973, J. Chem. Phys., 59, 4557
Loomis, R. A., Cleeves, L. I., Öberg, K. I., Guzman, V. V., & Andrews, S. M. 2015, ApJ, 809, L25
Loomis, R. A., Öberg, K. I., Andrews, S. M., et al. 2020, ApJ, 893, 101
Maeda, A., Medvedev, I. R., Winnewisser, M., et al. 2008, ApJS, 176, 543
Milam, S. N., Savage, C., Brewster, M. A., Ziurys, L. M., & Wyckoff, S. 2005, ApJ, 634, 1126
Müller, H. S. P., Schlöder, F., Stutzki, J., & Winnewisser, G. 2005, J. Mol. Struct., 742, 215
Noble, J. A., Theule, P., Mispelaer, F., et al. 2012, A&A, 543, A5
Öberg, K. I., & Bergin, E. A. 2016, ApJ, 831, L19
Öberg, K. I., Boamah, M. D., Fayolle, E. C., et al. 2013, ApJ, 771, 95
Öberg, K. I., Furuya, K., Loomis, R., et al. 2015a, ApJ, 810, 112
Öberg, K. I., Guzmán, V. V., Furuya, K., et al. 2015b, Nature, 520, 198
Oya, Y., & Yamamoto, S. 2020, ArXiv e-prints [arXiv:2010.01273]
Pacheco-Vázquez, S., Fuente, A., Baruteau, C., et al. 2016, A&A, 589, A60
Penteado, E. M., Walsh, C., & Cuppen, H. M. 2017, ApJ, 844, 71
Phuong, N. T., Chapillon, E., Majumdar, L., et al. 2018, A&A, 616, L5
Podio, L., Lefloch, B., Ceccarelli, C., Codella, C., & Bachiller, R. 2014, A&A, 565, A64
Podio, L., Bacciotti, F., Fedele, D., et al. 2019, A&A, 623, L6
Podio, L., Garufi, A., Codella, C., et al. 2020a, A&A, 642, L7
Podio, L., Garufi, A., Codella, C., et al. 2020b, A&A, 644, A119
Sakai, N., Oya, Y., López-Sepulcre, A., et al. 2016, ApJ, 820, L34
Schäfer, A., Horn, H., & Ahlrichs, R. 1992, J. Chem. Phys., 97, 2571
Schöier, F. L., van der Tak, F. F. S., van Dishoeck, E. F., & Black, J. H. 2005, A&A, 432, 369
Semenov, D., & Wiebe, D. 2011, ApJS, 196, 2
Semenov, D., Favre, C., Fedele, D., et al. 2018, A&A, 617, A28
Sheehan, P. D., & Eisner, J. A. 2017, ApJ, 840, L12
Sure, R., & Grimme, S. 2013, J. Comput. Chem., 34, 1672
Tatewaki, H., & Huzinaga, S. 1980, J. Comput. Chem., 1, 205
Teague, R., Henning, T., Guilloteau, S., et al. 2018, ApJ, 864, 133
Tieftrunk, A., Pineau des Forets, G., Schilke, P., & Walmsley, C. M. 1994, A&A, 289, 579
van 't Hoff, M. L. R., van Dishoeck, E. F., Jørgensen, J. K., & Calcutt, H. 2020, A&A, 633, A7
Wakelam, V., Caselli, P., Ceccarelli, C., Herbst, E., & Castets, A. 2004, A&A, 422, 159
Wakelam, V., Loison, J. C., Herbst, E., et al. 2015, ApJS, 217, 20
Wakelam, V., Ruaud, M., Hersant, F., et al. 2016, A&A, 594, A35
Wakelam, V., Bron, E., Cazaux, S., et al. 2017, Mol. Astrophys., 9, 1
Walsh, C., Millar, T. J., Nomura, H., et al. 2014, A&A, 563, A33
Walsh, C., Loomis, R. A., Öberg, K. I., et al. 2016, ApJ, 823, L10
Wiesenfeld, L., & Faure, A. 2013, MNRAS, 432, 2573
Wolf, S., Padgett, D. L., & Stapelfeldt, K. R. 2003, ApJ, 588, 373
Woodall, J., Agúndez, M., Markwick-Kemper, A. J., & Millar, T. J. 2007, A&A, 466, 1197
Wu, C.-J., Hirano, N., Takakuwa, S., Yen, H.-W., & Aso, Y. 2018, ApJ, 869, 59
Yen, H.-W., Gu, P.-G., Hirano, N., et al. 2019, ApJ, 880, 69